ASPS Conference Proceedings 1: 473-483 (2022)

Proceedings of

12th Structural Engineering Convention - An International Event (SEC 2022)

Available at https://asps-journals.com/index.php/acp

Effect of Carbon Steel Hollow Tubes as Reinforcement and Aluminum Foam as Shock Absorber on the Blast Response of One-way Concrete Slabs

S M Anas [1, *], Mehtab Alam [2], Md. I. Ansari [3]

[1] Department of Civil Engineering, Ph.D. Scholar, Jamia Millia Islamia, New Delhi, 110 025, India
[2] Department of Civil Engineering, Professor, Jamia Millia Islamia, New Delhi, 110 025, India
[3] Department of Civil Engineering, Assistant Professor, Jamia Millia Islamia, New Delhi, 110 025, India

Paper ID - 040435

Abstract

To investigate the blast response of the one-way normal strength concrete slabs reinforced on both sides with the High Yield Strength Deformed (HYSD) steel re-bars under air-blast loading, finite element (FE) simulation models have been developed using the explicit non-linear finite element program, ABAQUS/CAE. FE simulation outcomes are found matching closely with the available experimental results and observations. Analyses have been further extended substituting the hollow square carbon steel seamless tubes of grade Fe330 of equivalent strength in place of the conventional steel re-bars of grade Fe600 on the tension side, impact side only, and both the sides of the slab. The substitution has been considered to enhance the blast response of the slab. The damage has been simulated using the concrete damaged plasticity (CDP) model to evaluate the geometric parameters of cracks. The substitution of the tubes on the tension side only is found more effective in reducing the mid-span deflection, damage, and depth of transverse flexural cracks. Efforts have also been made to investigate the effectiveness of the aluminum foam as a shock absorber against the given level of the blast load. The use of two layers of the foam sandwiched with a thin steel sheet on the impact side of the slab only improves further the performance of the slab subjected to air-blast loading.

Keywords: Air-blast load, Concrete slab, Carbon steel hollow tubes, Aluminum foam, Explicit finite element analysis, Cracks, Damage, Damage dissipation energy

1. Introduction

Prior to recent explosive-induced havocs particularly in Beirut City of Lebanon, the blast-resistant design was primarily considered for the buildings such as embassies and other military facilities. Collapse of the buildings in the vicinity of the blast site and even damage to the structures at far distances has increased the concern of structural engineers for the safety of the buildings against blast-induced loadings. With another most recent accidental explosion triggered by sweeping glaze in a nearby field towards the ammunition depot in Ryazan (Russia) have got artillery shells exploding every 10 seconds [BBC News, CNN News]. It has been noticed that the level of damage to the structure from the blast could range from reparable to the collapse leading to the loss of lives. For the safety of the life and survival of the structures, a section of engineers is of the opinion that the structures in vulnerable zones should also be considered to design against such extreme loadings.

Both experimental and numerical investigations have been conducted to examine the damage resistance of to the different quantities of the TNT charges detonated at different scaled distances (between 0.75 and 3.0 m/kg$^{1/3}$) in the free air. Six out of the eight slabs were constructed with the reinforced concrete (RC) slabs under blast loading (Xu K. and Lu Y., 2006 [39]; Zhou Q. X. et al., 2008 [42]; Wu C. et al., 2009 [38]; Silva F. P. and Lu B., 2009 [27]; Tai S. Y. et al., 2011 [31]; Wang W. et al., 2012 [35]; Wang W. et al., 2013 [36]; Zhao F. C. and Chen Y. J., 2013 [41]; Lin X. et al., 2014 [20]; Thiagarajan G. et al., 2015 [33]; Feng J. et al., 2017 [6]; Kumar V. et al., 2020 [18]). *Low Y. H. and Hao H. (2002)* [21] developed two single-degree-of-freedom (SDOF) models to model the shear and flexural failure modes of the one-way RC slabs subjected to blast loading. Statistical variations of the concrete strengths, air-blast loading parameters, and structural dimensions were considered. The general conclusion drawn was that the chance of the survival of the slab in direct shear mode increases with the span length. Moreover, the slabs failed in a direct shear mode under the higher peak reflected blast pressures. *Wu C. et al. (2009)* [38] tested a total of eight RC slabs to investigate the damage resistance under the explosive-induced blast loading. The slabs were exposed the normal strength concrete, one slab constructed with the plain ultra-high-strength concrete, and one with the reinforced ultra-high-strength concrete. Two out of the six

*Corresponding author. Tel: +91-8527764166; E-mail address: mohdanas43@gmail.com

Published online: December 19, 2022
doi:10.38208/acp.v1.537

normal strength concrete slabs were retrofitted with the carbon fiber reinforced polymer (CFRP) sheets on the impact face only. The dimension of all the slabs was 2000 mm in length, 1000 mm in width, and 100 mm in depth. The slabs were doubly reinforced with the 12 mm diameter High Yield Strength Deformed (HYSD) steel re-bars. The reinforcement was provided on both compression and tension sides at a spacing of 200 mm c/c in the minor bending plane (#12 mm @ 200 mm c/c) and 100 mm c/c in the other plane (#12 mm @ 100 mm c/c). The yield strength, ultimate tensile strength, Young's modulus, and Poisson's ratio of the reinforcing bars were 600 MPa, 660 MPa, 210 GPa, and 0.28, respectively. The thickness of the concrete cover was 10 mm. The 28-day average cylinder compressive strength of the normal strength concrete was 39.50 MPa, while that of the ultra-high-strength concrete was 150 MPa. Results revealed that the energy absorption capacity of the plain ultra-high-strength concrete slab was comparable to that of the normal reinforced concrete slab, however, the energy absorption capacity of the reinforced ultra-high-strength concrete slab was found superior to both the slabs. *Ohkubo K. et al. (2008)* [24] experimentally investigated the effectiveness of carbon- and aramid- fiber sheets on the blast performance of the 500 mm x 500 mm x 100 mm one-way concrete plates subjected to the contact explosion. The explosive charge was considered Composition 4 (90:10 RDX: Poly-isobutylene). The compressive strength of the concrete was 22.30 MPa. Carbon and aramid fiber sheets were glued on the bottom tension side of the concrete plate using epoxy adhesive. It was reported that the concrete plate with a double layer of the aramid fiber sheet on the bottom surface was more effective in reducing the damage and cracks in comparison to that with two layers of the carbon fiber sheet on the rear side. *Silva F. P. and Lu B. (2009)* [27] conducted explosion tests to study the influence of the charge weight and the detonation distance on the damage resistance of 1200 mm x 1200 mm x 90 mm one-way RC slabs under blast loading. A total of the eight slabs were cast with 27.60 MPa concrete and were exposed to the spherical-shaped explosive charges (RDX) at standoff distances of 0.30 and 0.90 m in free air. The yield strength, ultimate tensile strength, and elastic modulus of the reinforcing bars were 414 MPa, 621 MPa, and 200 GPa, respectively. Four damage levels were obtained as follows: (1) Level I (Yielding of the reinforcement, crack width < 1 mm); (2) Level II (Initiation of plastic deformation, the formation of diagonal cracks, crack width < 2 mm); (3) Level III (Visible permanent deformations, crack width < 2 mm); and (4) Level IV (Rupturing of the reinforcement, crack width > 2 mm). A six-step methodology was developed using the displacement-based design (DBD) method to predict damage levels of the slab for the given level of blast load. However, the proposed methodology was not applicable when the response of the slab was governed by the punching-shear failure mode. *Wang W. et al. (2013)* [36] conducted blast tests to investigate the damage modes of four 1000 mm x 1000 mm x 40 mm one-way RC slabs exposed to the different quantities of the TNT charges detonated at different scaled distances (between 0.488 and 0.684 m/kg$^{1/3}$) in free air. All the slabs were cast with 39.50 MPa normal strength concrete. The slabs were isotopically reinforced with the High Yield Strength Deformed steel re-bars of diameter 6 mm at a fixed spacing of 75 mm c/c. The experimental results were compared and found to be in reasonable agreement with the predictions of LS-DYNA software. Four damage modes of the RC slab were obtained namely; flexural failure mode, spallation mode, perforation mode, and punching-shear failure mode. *Yao S. et al. (2016)* [40] experimentally and numerically investigated the effect of the reinforcement ratio on the damage resistance of 850 mm x 750 mm x 30 mm one-way RC slabs under close-in blast loading. A total of the six slabs were cast with 39.50 MPa concrete. Two sets of the blast tests were conducted under 0.13 and 0.19 kg TNT charge with three different reinforcement ratios (0.44%, 2.42%, and 3.76%) in each set. All the slabs were isotopically reinforced with the 6 mm diameter steel re-bars of grade HPB235. The obvious conclusion drawn was that the damage degree, mid-span deflection, and the concrete spall radius all were reduced significantly with the increase of the reinforcement ratio. *Kumar V. et al. (2020)* [18] conducted blast tests to investigate the damage resistance of 1000 mm x 1000 mm x 100 mm one-way RC slabs. A total of the six slabs were tested and subjected to the cylindrical-shaped explosive charges ranging from 0.85 to 2.0 kg detonated at standoff distances of 0.10 m and 0.50 m in free air. The slabs were isotopically reinforced with the 10 mm diameter steel re-bars of grade Fe500 (IS 1786:2008). The results were compared and found to be in good agreement with the predictions of the Holmquist-Johnson-Cook (HJC) concrete material model available in the ABAQUS finite element program. They observed that the impact side (top face) of the RC slab failed due to the compressive failure and formation of the crater, while the rear side of the slab failed with the concrete spalling under the higher level of blast load.

In the present work, efforts have been made to improve the blast resistance capacity of the RC slabs substituting the hollow square carbon steel tubes of grade Fe330 of equivalent strength in place of the conventional steel re-bars of grade Fe600 on the tension side, impact side only, and both the sides of the slab. A sophisticated concrete material model has been utilized to evaluate the geometric parameters of cracks. The goals of the present investigation are:

1. To develop finite element simulation models of the normal strength concrete slab, reinforced on both compression and tension sides with the HYSD steel re-bars, tested by Wu C. et al. (2009) [38] under different peak overpressures;
2. To validate FE simulation results with the available experimental values;
3. To find out the best placement of the reinforcements by substituting the conventional steel reinforcement with the square steel tubes of equivalent yield strength on the tension side, impact side only, and both the sides of the slab;
4. To investigate the role of aluminum metal foam as a shock absorber against air-blast loading; and
5. To evaluate geometric parameters of cracks for the considered substitutions of the steel tubes and scaled distances.

2. Numerical Modeling

In the current study, FE simulation models of the normal reinforced concrete slab tested by Wu C. et al. (2009) [38] have been developed using ABAQUS/CAE commercial program. Fig.-1 shows the dimensions and reinforcement details of the slabs. The FE models are subjected to the different quantities of the TNT charges at different scaled distances (between 0.75 and 3.0 m/kg$^{1/3}$) in free air. An explicit solver in the ABAQUS/CAE has been employed to simulate the blast response of the slabs. The concrete is discretized with 8-node explicit solid elements (C3D8R) with hourglass control and reduced integration (ABAQUS User Assistance Manual, 2017). The re-bars are discretized with 3-node explicit second-order beam elements (B32). The re-bars are embedded into the concrete slab using embedded region constraint (see Fig.-2). The short edges of the slab are assumed constrained in all degrees of freedom. A mesh size of 10 mm has been adopted following the convergence test conducted at two different scaled distances (0.75 and 3.0 m/kg$^{1/3}$). The final mesh has 225,315 nodes and 200,440 elements (see Fig.-3).

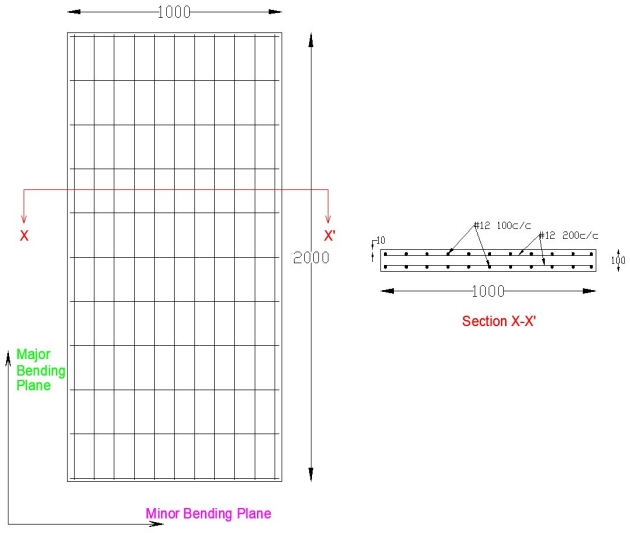

Fig. 1. Dimensions (mm) and reinforcement details of the slabs tested by Wu C. et al. (2009) [38]

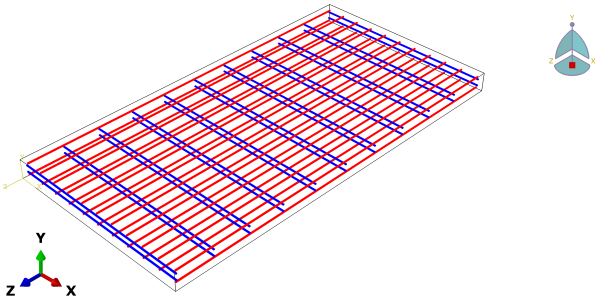

Fig. 2. Rendered view of the steel re-bars

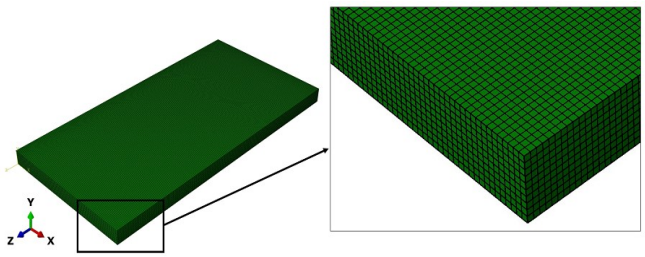

Fig. 3. FE mesh

2.1 Steel tubes properties

UNI 8863(1987) Grade Fe330 hollow square carbon steel seamless tubes have been considered in the present work. UNI 8863 Grade Fe330 tubes are low-cost low carbon steel tubes with max 0.17% carbon content with a combination of max 0.65% manganese. The dimensions of the tubes are shown in Fig.-4. The mass density, yield strength, ultimate tensile strength, and ultimate percentage elongation of the tubes are 7855 kg/m^3, 330 MPa, 520 MPa, and 22%, respectively. The tubes are embedded into the concrete slab using embedded region constraint. Fig.-5 shows the rendered views of the reinforcement.

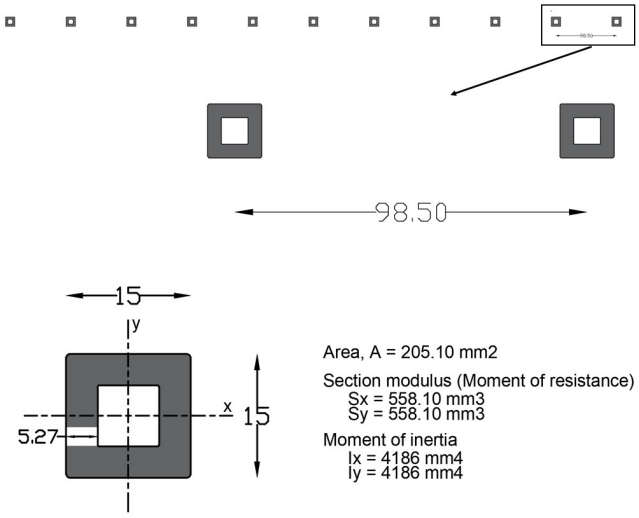

Fig. 4. Dimensions of the tubes in "mm"

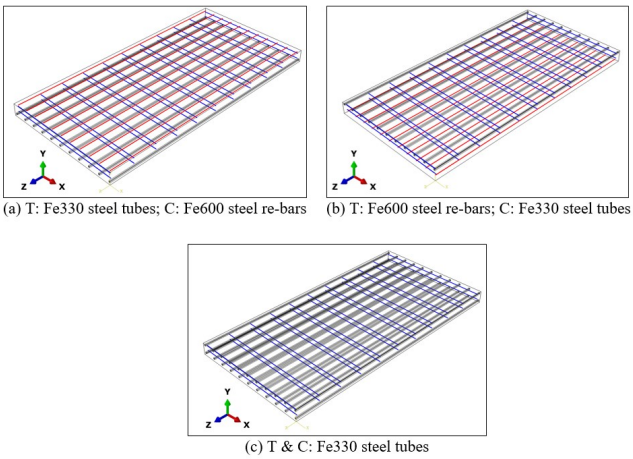

Fig. 5. Rendered views of the reinforcement

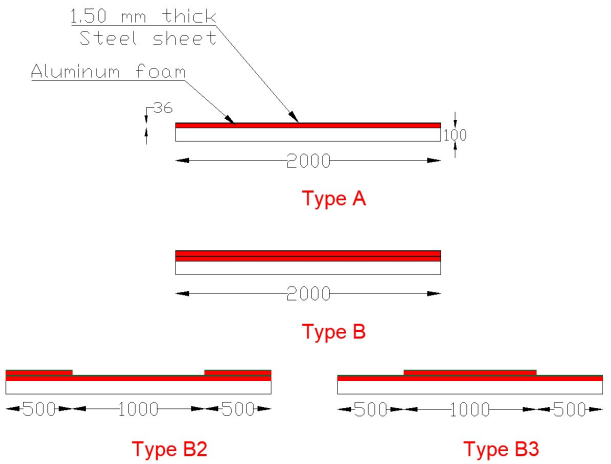

Fig. 6. Different schemes of the aluminum foam

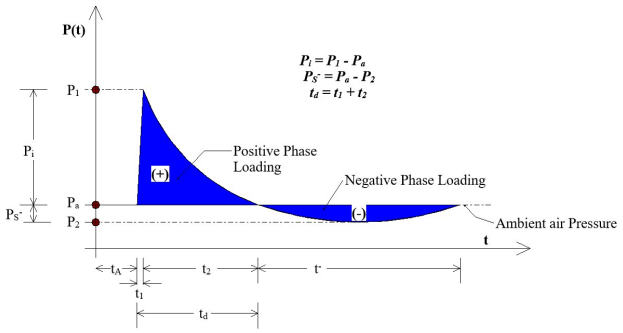

Fig. 7. Typical blast pressure profile [37]

2.2 *Aluminum foam properties*

In the present work, closed-cell aluminum foams are used and are applied on the top surface (blast face) of the target slab in different ways as shown in Fig.-6. The protected substitution layers of the aluminum foam are covered by a thin structural steel sheet (see Fig.-6). The input parameters including mass density, Young's modulus, simple shear test data, and uniaxial test data of the aluminum foam have been taken from the experimental study conducted by Schenker A. et al. (2008) [25]. The thickness of the metallic foam used is 36 mm. A surface-to-surface contact interaction, with "friction", "cohesive", and "hard" contact models, has been utilized to define the interaction between two surfaces namely; the master surface, and the slave surface [1]. Besides, the kinematic contact method with finite sliding has been adopted for the mechanical contact formulation [1]. Aluminum foams are discretized with 8-node explicit solid elements (C3D8R) with reduced integration and hourglass control (ABAQUS User Assistance Guide, 2017). A mesh size of 9 mm has been adopted for the aluminum foam following the convergence test conducted at a scaled distance of 0.75 m/kg$^{1/3}$.

2.3 *Air-blast loading, P(t)*

Fig.-7 shows the typical explosive-induced air-blast pressure-time history produced from the ideal explosion, proposed by Wu C. and Hao H. (2005) [37]. In general, explosive-induced blast load is characterized by two phases namely; the positive phase, and the negative phase [3, 8, 15]. In the negative phase, the blast pressure falls below the ambient air pressure and a partial vacuum is formed. Current design guidelines for the blast protective structures usually recommend utilizing only the positive pressure phase of the blast load by assuming that the negative phase is normally much weaker and does not affect typical concrete structures [11]. Thus, the effect of the suction phase of the blast load on the blast response of the slabs has been neglected in the current study.

Wu C. and Hao H. (2005) [37] experimentally investigated the effects of air-blast load and ground shock on concrete structures, and proposed several empirical equations to compute blast and ground shock wave parameters. They compared their results and found in good agreement with the predictions of TM 5-1300 (1990), *Structures to resist the effects of Accidental Explosions* [15]. Moreover, they simplified the positive phase of air-blast load into three parts: a constant ambient air pressure (P_a) followed by a sudden linear rise in air pressure to the peak value at the pressure front and then an exponential decay of the varying pressure, P(t). The following are the equations proposed by Wu C. and Hao H. (2005) [37] to define or model the time-dependent blast pressure, P(t):

$$t_A = 0.34\, R^{1.4}\, Q^{-0.2} / C_a \tag{1}$$

$$t_d = t_1 + t_2 \tag{2}$$

$$t_1 = 0.0019 \left(\frac{R}{Q^{\frac{1}{3}}}\right)^{1.30} \tag{3}$$

$$t_2 = 0.0005\, R^{0.72}\, Q^{0.16} \tag{4}$$

$$P(t) = \begin{cases} P_a; & (0 \le t < t_A) \\ P_a + P_i\left(\frac{t}{t_1}\right); & (t_A \le t \le t_1) \\ P_a + P_i\left(1 - \frac{t-t_1}{t_2}\right).exp\left(-\frac{\gamma(t-t_1)}{t_2}\right); & (t_1 \le t) \end{cases} \tag{5}$$

Here, Q = Weight of the charge (kg TNT); R = detonation distance (m); C_a = Speed of sound in air (≈340 m/sec); t_A = time of arrival of shock wave (sec); t_1 = rising time (sec); t_2 = decreasing time (sec); t_d = duration of positive phase of blast load (sec); P_a = ambient pressure (≈0.1 MPa); P_i = incident overpressure or peak overpressure (MPa); Z = scaled distance (R/Q$^{1/3}$, m/kg$^{1/3}$); and γ = decay of the curve. The decay constant (γ) can be calculated using the following equations [37]:

$$\gamma = \begin{cases} 3.02\, P_i^{0.38} + 6.85\, P_i^{0.79}.exp\left(-4.55\frac{t-t_1}{t_2}\right); & (t_1 \le t \le t_d) \\ 1.96\, P_i^{0.25} + 0.176\, P_i.exp\left(-0.73\, P_i^{-0.49}.\left(\frac{t-t_d}{t_2}\right)\right); & (t_d < t) \end{cases} \tag{6}$$

for P_i (MPa) ≦ 1.0,

$$\gamma = \begin{cases} 1.62\, P_i^{0.30} + 5.13\, P_i^{0.28}.exp\left(-1.05\, P_i^{0.37}.\left(\frac{t-t_1}{t_2}\right)\right); & (t_1 \le t \le t_d) \\ 0.74\, P_i^{0.17} + 2.71\, P_i^{0.28}.exp\left(-0.26\, P_i^{0.33}.\left(\frac{t-t_1}{t_2}\right)\right); & (t_d < t) \end{cases} \tag{7}$$

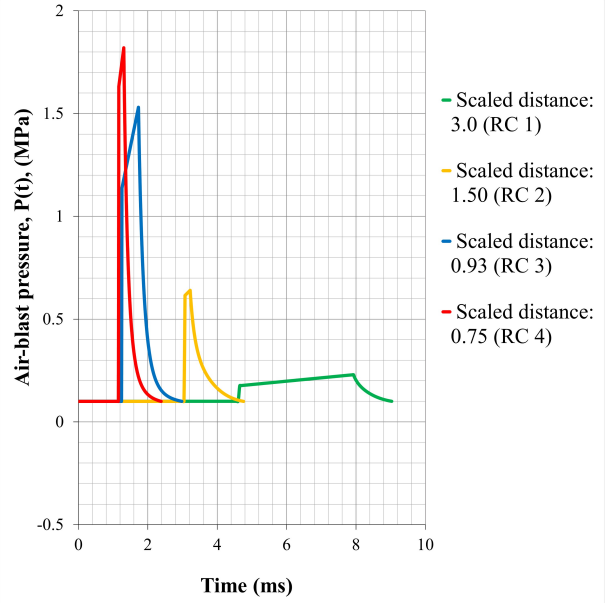

Fig. 8. Estimated blast pressure-time histories

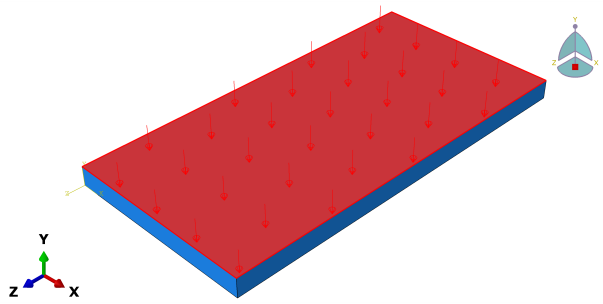

Fig. 9. Load application of the blast pressure, P(t)

Table-1. Estimated values of air-blast wave parameters

Slab ID	Z (m/kg$^{1/3}$)	P_i (MPa)	t_A (ms)	t_l (ms)	t_d (ms)	Total duration, $t = t_A + t_d$ (ms)
RC 1	3.00	0.13	4.66	3.29	4.39	9.05
RC 2	1.50	0.54	3.08	0.16	1.70	4.78
RC 3	0.93	1.43	1.26	0.49	1.74	3.00
RC 4	0.75	1.72	1.17	0.16	1.23	2.40

for $1.0 \leqslant P_i$ (MPa) $\leqq 100$. The values of incident blast pressure (P_i) for different scaled distances have been taken from the experimental study conducted by Wu C. (2009) [38]. The estimated values of blast wave parameters are summarized in Table-1. Fig.-8 shows the estimated air-blast pressure profiles. The air-blast loading in ABAQUS/CAE program has been defined as pressure versus time application using an explicit solver. The blast pressure, P(t) has been applied to the top surface (impact face) of the target slab as shown in Fig.-9.

2.4 Material model

Numerous constitutive models for the concrete have been developed to simulate the non-linear behavior of the concrete due to crushing in compression and cracking in tension (Ju W. J., 1989 [16]; Lee J. and Fenves L. G., 1998 [19]; Grassl P. and Jirasek M., 2006 [9]; Jason L. et al., 2006 [14]; Valentini B. and Hofstetter G., 2011 [34]). A very popular constitutive model is the concrete damaged plasticity model that combines plasticity and damage-mechanics theories [12]. In the present study, the concrete damaged plasticity (CDP) model available in the ABAQUS/CAE software has been employed to simulate the damage and to evaluate geometric parameters of cracks under the considered blast loading. The CDP model is a modification of the Drucker-Prager model proposed by Lubliner J. et al. (1989) [22] and Lee J. (1998) [19]. The evolution of the failure surface is controlled by two damage variables namely; compressive damage (d_c) and tensile damage (d_t), which are connected to failure mechanisms of the concrete under compression and tension loadings [1, 12]. It is assumed that the uniaxial stress-strain curves can be converted into stress versus inelastic-strain curves [1]. This conversion is performed automatically by the ABAQUS/CAE program from the user-provided stress versus plastic strain data. The uniaxial compressive and tensile responses of the material with respect to the CDP model under compression and tension loadings are given by:

$$\sigma_c = (1 - d_c)E_0(\varepsilon_c - \varepsilon_c^{pl,\ h}) \quad (8)$$

$$\sigma_t = (1 - d_t)E_0(\varepsilon_t - \varepsilon_t^{pl,\ h}) \quad (9)$$

Here, σ_c = nominal compressive stress; σ_t = nominal tensile stress; ε_c = Compressive strain ($\varepsilon_c^{pl,\ h} + \varepsilon_c^{el}$); ε_t = Tensile strain ($\varepsilon_t^{pl,\ h} + \varepsilon_t^{el}$); $\varepsilon_c^{pl,\ h}$ = plastic hardening compressive strain; $\varepsilon_t^{pl,\ h}$ = plastic hardening tensile strain; ε_c^{el} = elastic compressive strain; ε_t^{el} = elastic tensile strain; E_0 = initial elasticity modulus of material (undamaged); d_c and d_t are compression and tension damage variables ranging from zero (undamaged material) to one (total loss of strength). The non-linear properties of concrete (39.50 MPa) taken from Hafezolghorani M. et al. (2017) [12] are tabulated in Table-2, where "ψ" is the dilation angle, "ε" is the flow potential eccentricity, "f_{b0} / f_{c0}" is the ratio of initial biaxial to initial uniaxial compressive yield stress, "K" is the ratio of the second stress invariant on the tensile meridian to that on the compressive meridian, and "μ" is the viscosity parameter.

Table-2. CDP material parameter table for the concrete [12]

ψ	ε	f_{b0} / f_{c0}	K	μ
31°	0.10	1.16	0.67	0

Compressive Behavior		Compression Damage	
Yield Stress (MPa)	Inelastic Strain	Yield Stress (MPa)	Inelastic Strain
20.40	0	0	0
25.60	2.66667E-05	0	2.66667E-05
30.00	0.00008	0	0.00008
33.60	0.00016	0	0.00016
36.40	0.00026666	0	0.00026666
38.40	0.0004	0	0.0004
39.60	0.00056	0	0.00056
40.00	0.00074666	0	0.00074666
39.60	0.00096	0.01	0.00096
38.40	0.0012	0.04	0.0012
36.40	0.00146666	0.09	0.00146666
33.60	0.00176	0.16	0.00176
30.00	0.00208	0.25	0.00208
25.60	0.00242666	0.36	0.00242666
20.40	0.0028	0.49	0.0028
14.40	0.0032	0.64	0.0032
7.60	0.00362666	0.81	0.00362666
Tensile Behavior		Tension Damage	
Yield Stress (MPa)	Cracking Strain	Yield Stress (MPa)	Cracking Strain
4.00	0	0	0
0.04	0.00133333	0.99	0.00133333

3. Results and Discussion

3.1. Validation of FE simulation results

In order to validate the accuracy of the employed non-linear finite element program, maximum mid-span deflections and pattern of cracks generated from the finite element analysis are compared with the results of Wu C. et al. (2009) [38]. Comparisons of crack patterns obtained from the CDP model and Wu C. (2009) are shown in Fig.-10. Comparisons of maximum mid-span deflection obtained from FE analysis and Wu C. (2009) [38] are listed in Table-3. The pattern of cracks and maximum mid-span deflections obtained from the FE analysis are in good agreement with available experimental results and the average deviation is less than 3.0%. The reasonable difference indicates that the employed FE program can give a reliable prediction of maximum mid-span deflection and damage in the slabs subjected to explosive-induced air-blast loading.

3.2. Replacement of the steel re-bars by the tubes of equivalent strength

Following a good correlation between FE simulation and available experimental results, further analysis has been conducted substituting the hollow square carbon steel tubes of grade Fe330 of equivalent strength in place of the conventional steel re-bars of grade Fe600 on the tension side, impact side only, and both the sides of the slab. The substitution has been considered to improve the blast resistance capacity of the slabs. Table-4 summarizes the maximum mid-span deflection in the slabs. The deflection

Table-3. Comparison of maximum deflections

Slab No.	Q (kg)	Z (m/kg$^{1/3}$)	Maximum mid-span deflection in the slab (mm)		Percentage difference (%)
			Experimental result (Wu C. et al., 2009)	FEA result	
RC 1	1.00	3.00	1.50	1.54	2.63
RC 2	8.00	1.54	10.50	10.44	0.57
RC 3	3.44	0.93	13.90	13.04	6.38
RC 4	8.00	0.75	38.90	38.57	0.85

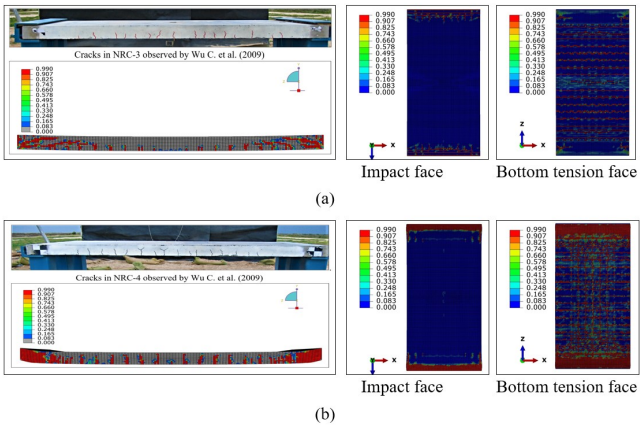

Fig. 10. Comparison of crack patterns for concrete slabs with steel re-bars on both faces: (a) RC 3 (t=3.00 ms), and (b) RC 4 (t=2.40 ms)

time histories of the different specimens are shown in Fig.-11. The distribution of deflection for the considered substitutions of the steel tubes is shown in Fig.-12. In this study, the damage in the slabs has been observed in the form of concrete crushing near supports led by flexural-shear failure, development of transverse flexural and flexural-shear cracks on the bottom tension side, and damage dissipation energy. Table-5 summarizes the damage dissipation energy in the slabs. The damage dissipation energy in the slabs is significantly reduced with the replacement of conventional steel re-bars by the carbon steel tubes of equivalent strength (Table-5). The reduction in the damage dissipation energy indicates that the slab suffered lesser damage with the substitution of the tubes (Table-4&5). The reason why tubes are more effective to the local damage than the steel re-bars is inferred that the flexural rigidity (EI) of one tube is 4.12 times larger than that of one steel re-bar. The geometric parameters of cracks for the different specimens and substitutions are listed in Table-6to10. The distributions of cracks on the bottom tension side, impact face, and along the span of the slab RC 4 for the considered substitutions are shown in Fig.-13, Fig.-14, and Fig.-15, respectively. For the considered substitutions of the tubes, the concrete slab with the steel re-bars on the tension side and the tubes on the compression side gives the poorest performance under the applied blast pressures (Table-4&5). The concrete slab reinforced with the steel re-bars on the impact side and the tubes of equivalent strength on the tension side decreased the mid-span deflection by approximately 27%, damage dissipation energy by 42%, and depth of transverse flexural cracks by 42%, while the slab with the tubes on both sides reduced the mid-span deflection by 45%, damage dissipation energy by 48%, and depth of flexural cracks by 29% (approx..) in comparison to the slab with the steel re-bars on both sides. Although, reduction of deflection and damage dissipation energy is maximum for the 100% replacement of the conventional steel re-bars by the tubes of equivalent strength on both the sides of the slab, yet 100% substitution by the tubes of equivalent strength on the tension side only is found to be a more effective substitution with regards to the cracking resistance against the applied air-blast loading (Table-4,5&9).

FE simulation results show that slabs only suffer flexural deformation. With the decrease of proximity factor (Z), the damage mode changes from the formation of flexural cracks on the rear side (tension side) to the development of longitudinal, flexural-shear, and flexural cracks on both the sides of the slab (Table-11). Also, crushing of concrete led by flexural-shear failure occurred near the supports of the slab RC 4 which is subjected to blast pressure of 1.72 MPa at a scaled distance of 0.75 m/kg$^{1/3}$ (see Fig.-13&14).

3.3. Effectiveness of aluminum foam to improve the damage resistance of the slab

In order to determine the effectiveness of aluminum foam as a blast protective layer, analysis has been conducted on the concrete slab reinforced with the Fe600 steel re-bars on the compression side and the Fe330 carbon steel hollow tubes on the tension side. Single and double layers of the aluminum foam covered by a thin steel sheet are applied in

different ways to the top surface of the target slab as shown in Fig.-6. The results show that the unprotected slab experienced more mid-span deflection and damage than the slab protected with the aluminum foams (see Fig.-13,16&17). Higher compression of the foam in single and double layers near the supports of the slab has been observed because of the lesser deflection of the slab over the regions (see Fig.-17). An additional single protecting layer of aluminum foam with steel sheet (Type A) decreased the deflection in the target slab by approximately 15% and depth of transverse flexural cracks by 13% (Table-12&14). The concrete slab reinforced with the steel re-bars on the compression side with a double layer of aluminum foam and sheet (Type B) and with the tubes on the tension side reduced the mid-span deflection by approximately 33%, damage dissipation energy by 90%, and depth of flexural cracks by 40% (Table-12to14). Two layers of aluminum foam and sheet at the quarter-span and a single layer at the mid-span (Type B2) of the target slab reduced the mid-span deflection by 14% and crack depth by 18% (approx..). Moreover, the concrete slab reinforced with the Fe600 steel re-bars on the compression side with two layers of the foam and sheet at the mid-span and a single layer at the quarter-span (Type B3) and with the Fe330 steel tubes on the tension side reduced the mid-span deflection by approximately 24%, damage dissipation energy by 69%, and depth of transverse flexural cracks by 28% (Table-12&14). Thus, the double layer of the foam along with the steel sheet is immensely effective in enhancing the damage resistance of the slab as compared to single layer of the foam and sheet.

Table-4. Summary of maximum deflection in the slabs

Reinforcement	Maximum mid-span deflection in the slabs (mm)			
	RC 1	RC 2	RC 3	RC 4
C & T: Fe600 steel re-bars	1.54	10.44	13.04	38.57
C: Fe600 steel re-bars T: Fe330 hollow carbon steel tubes	0.96 (^{a}38%)	7.73 (^{a}26%)	9.58 (^{a}27%)	32.38 (^{a}16%)
C: Fe330 hollow carbon steel tubes T: Fe600 steel re-bars	1.01 (^{a}34%)	8.56 (^{a}18%)	10.89 (^{a}16%)	33.93 (^{a}12%)
C & T: Fe330 hollow carbon steel tubes	0.59 (^{a}62%)	5.29 (^{a}49%)	7.04 (^{a}46%)	28.67 (^{a}26%)

* ^{a} Percentage decrease with respect to the slab with Fe600 steel re-bars on both the sides (%)
* *C* Compression side (Blast face)
* *T* Tension side

Table-5. Summary of damage dissipation energy in the slabs

Reinforcement	Cumulative damage dissipation energy (J)			
	RC 1	RC 2	RC 3	RC 4
C & T: Fe600 steel re-bars	87.90	1679.25	7703.35	64070.65
C: Fe600 steel re-bars T: Fe330 hollow carbon steel tubes	59.33 (^{a}33%)	715.56 (^{a}57%)	4136.84 (^{a}46%)	44849.40 (^{a}30%)
C: Fe330 hollow carbon steel tubes T: Fe600 steel re-bars	65.66 (^{a}25%)	1339.42 (^{a}20%)	7430.55 (^{a}4%)	59954.01 (^{a}6%)
C & T: Fe330 hollow carbon steel tubes	48.41 (^{a}45%)	588.19 (^{a}65%)	3811.44 (^{a}51%)	42927.30 (^{a}33%)

* ^{a} Percentage decrease with respect to the slab with Fe600 steel re-bars on both the sides (%)
* *C* Compression side (Impact face)
* *T* Tension side

Table-6. Average spacing of transverse cracks in slab RC 2 for the considered substitutions of the steel tubes

Reinforcement	Average spacing of transverse cracks (mm)			
	Impact face		Tension face	
	Q_{Span} (L/4)	M_{Span}	Q_{Span} (L/4)	M_{Span}
C & T: Fe600 steel re-bars	f (^{g}90)	-	-	67 (^{m}15, ^{g}40)
C: Fe600 steel re-bars T: Fe330 hollow carbon steel tubes	f (^{g}75)	-	-	56 (^{m}13, ^{g}27)
C: Fe330 hollow carbon steel tubes T: Fe600 steel re-bars	100 (^{m}2, ^{g}60)	-	-	78 (^{m}12, ^{g}47)
C & T: Fe330 hollow carbon steel tubes	100 (^{m}2, ^{g}60)	-	-	30 (^{m}16, ^{g}38)

* Q_{Span} Quarter-span * M_{Span} Mid-span
* ^{m} Number of cracks developed * ^{g} Average depth of cracks (mm)
* ^{f} Flexural shear crack near supports

Table-7. Average spacing of longitudinal cracks in slab RC 3 for the considered substitutions of the steel tubes

Reinforcement	Average spacing of longitudinal cracks (mm)			
	Impact face		Tension face	
	W/4	W/2	W/4	W/2
C & T: Fe600 steel re-bars	35 (^{m}3, ^{g}30)	120 (^{m}4, ^{g}20)	10 (^{m}2, ^{g}20)	-
C: Fe600 steel re-bars T: Fe330 hollow carbon steel tubes	-	-	-	-
C: Fe330 hollow carbon steel tubes T: Fe600 steel re-bars	57 (^{m}4, ^{g}35)	380 (^{m}2, ^{g}17)	-	-
C & T: Fe330 hollow carbon steel tubes	-	-	-	-

* ^{m} Number of cracks developed * ^{g} Average depth of cracks (mm)

Table-8. Average spacing of transverse cracks in slab RC 3 for the considered substitutions of the steel tubes

Reinforcement	Average spacing of transverse cracks (mm)			
	Impact face		Tension face	
	Q_{Span} (L/4)	M_{Span}	Q_{Span} (L/4)	M_{Span}
C & T: Fe600 steel re-bars	23 (^{m}4, ^{g}50)	-	54 (^{m}7, ^{g}58)	63 (^{m}14, ^{g}49)
C: Fe600 steel re-bars; T: Fe330 hollow carbon steel tubes	-	-	30 (^{m}4, ^{g}38)	90 (^{m}13, ^{g}29)
C: Fe330 hollow carbon steel tubes T: Fe600 steel re-bars	70 (^{m}2, ^{g}70)	-	25 (^{m}5, ^{g}60)	80 (^{m}12, ^{g}48)
C & T: Fe330 hollow carbon steel tubes	90 (^{m}2, ^{g}65)	-	60 (^{m}3, ^{g}37)	55 (^{m}13, ^{g}37)

* ^{m} Number of cracks developed * ^{g} Average depth of cracks (mm)

Table-9. Average spacing of transverse cracks in slab RC 4 for the considered substitutions of the steel tubes

Reinforcement	Average spacing of transverse cracks (mm)			
	Impact face		Tension face	
	Q_{Span} (L/4)	M_{Span}	Q_{Span} (L/4)	M_{Span}
C & T: Fe600 steel re-bars	h (^{g}98)	-	35 (^{m}10, ^{g}80)	87 (^{m}16, ^{g}85)
C: Fe600 steel re-bars T: Fe330 hollow carbon steel tubes	h (^{g}90)	-	28 (^{m}7, ^{g}74)	85 (^{m}9, ^{g}40)
C: Fe330 hollow carbon steel tubes T: Fe600 steel re-bars	80 (^{m}4, ^{g}95)	-	31 (^{m}10, ^{g}83)	84 (^{m}11, ^{g}58)
C & T: Fe330 hollow carbon steel tubes	100 (^{m}2, ^{g}93)	-	23 (^{m}11, ^{g}82)	82 (^{m}11, ^{g}45)

* Q_{Span} Quarter-span * M_{Span} Mid-span
* ^{m} Number of cracks developed * ^{g} Average depth of cracks (mm)
* ^{h} Crushing of concrete led by flexural-shear failure at supports

Table-10. Average spacing of longitudinal cracks in slab RC 4 for the considered substitutions of the steel tubes

Reinforcement	Average spacing of longitudinal cracks (mm)			
	Impact face		Tension face	
	W/4	W/2	W/4	W/2
C & T: Fe600 steel re-bars	85 (^{m}3, ^{g}100)	-	80 (^{m}7, ^{g}85)	85 (^{m}8, ^{g}73)
C: Fe600 steel re-bars T: Fe330 hollow carbon steel tubes	70 (^{m}3, ^{g}30)	180 (^{m}3, ^{g}30)	50 (^{m}3, ^{g}30)	67 (^{m}4, ^{g}45)
C: Fe330 hollow carbon steel tubes T: Fe600 steel re-bars	10 (^{m}2, ^{g}20)	-	85 (^{m}3, ^{g}40)	90 (^{m}5, ^{g}57)
C & T: Fe330 hollow carbon steel tubes	25 (^{m}5, ^{g}33)	10 (^{m}2, ^{g}92)	25 (^{m}5, ^{g}50)	74 (^{m}6, ^{g}70)

$*^{m}$ Number of cracks developed $*^{g}$ Average depth of cracks (mm)

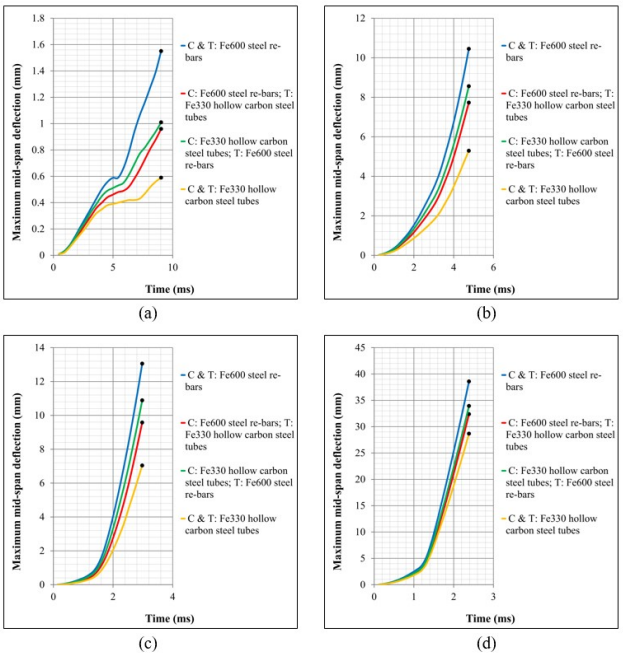

Fig. 11. Deflection – time histories of different specimens: (a) RC 1 (t=9.05 ms), (b) RC 2 (t=4.78 ms), (c) RC 3 (t=3.00 ms), and (d) RC 4 (t=2.40 ms)

Table-11. Observed damage levels

Slab No.	Z (m/kg$^{1/3}$)	Damage level	Remarks
RC 1	3.00	Low	• No cracking
RC 2	1.54	Moderate	• Few flexural-shear cracks on the impact face near the supports; • Transverse flexural cracks on the tension side at the mid-span; • No concrete crushing
RC 3	0.93	High	• Formation of flexural-shear and flexural cracks on the tension side; • Few transverse cracks on the impact face near the supports; • No concrete crushing
RC 4	0.75	Very high	• Crushing of concrete near supports led by flexural-shear failure; • Few longitudinal cracks on the blast face; • Significant number of flexural-shear and flexural cracks on the tension side;

Table-12. Summary of deflection in slab RC 4 without and with aluminum foam

Reinforcement	Maximum mid-span deflection in slab RC 4 (mm)
C & T: Fe600 steel re-bars	38.57
C: Fe600 steel re-bars T: Fe330 hollow carbon steel tubes	32.38
C: Fe600 steel re-bars + Aluminum Foam (Type A) T: Fe330 hollow carbon steel tubes	27.41 (^{a}29% ; ^{b}15%)
C: Fe600 steel re-bars + Aluminum Foam (Type B) T: Fe330 hollow carbon steel tubes	21.63 (^{a}44% ; ^{b}33%)
C: Fe600 steel re-bars + Aluminum Foam (Type B2) T: Fe330 hollow carbon steel tubes	27.71 (^{a}28% ; ^{b}14%)
C: Fe600 steel re-bars + Aluminum Foam (Type B3) T: Fe330 hollow carbon steel tubes	24.58 (^{a}36% ; ^{b}24%)

$*^{a}$ Percentage decrease with respect to the slab with Fe600 steel re-bars on both the sides (%)
$*^{b}$ Percentage decrease with respect to slab with Fe600 steel re-bars on compression side and Fe330 hollow carbon steel tubes on tension side (%)
$*$ *C* Compression side (Blast face)
$*$ *T* Tension side

Table-13. Summary of damage dissipation energy in slab RC 4 without and with aluminum foam

Reinforcement	Cumulative damage dissipation energy (J)
C & T: Fe600 steel re-bars	64070.65
C: Fe600 steel re-bars T: Fe330 hollow carbon steel tubes	44849.40
C: Fe600 steel re-bars + Aluminum Foam (Type A) T: Fe330 hollow carbon steel tubes	26867.08 (^{a}58% ; ^{b}40%)
C: Fe600 steel re-bars + Aluminum Foam (Type B) T: Fe330 hollow carbon steel tubes	4622.55 (^{a}93% ; ^{b}90%)
C: Fe600 steel re-bars + Aluminum Foam (Type B2) T: Fe330 hollow carbon steel tubes	24346.85 (^{a}62% ; ^{b}46%)
C: Fe600 steel re-bars + Aluminum Foam (Type B3) T: Fe330 hollow carbon steel tubes	13693.26 (^{a}79% ; ^{b}69%)

$*^{a}$ Percentage decrease with respect to the slab with Fe600 steel re-bars on both the sides (%)
$*^{b}$ Percentage decrease with respect to slab with Fe600 steel re-bars on compression side and Fe330 hollow carbon steel tubes on tension side (%)

Table-14. Average spacing of transverse flexural cracks in slab RC 4 without and with aluminum foam

Reinforcement	Average spacing of transverse flexural cracks (mm)
C & T: Fe600 steel re-bars	87 (^{m}16, ^{g}85)
C: Fe600 steel re-bars T: Fe330 hollow carbon steel tubes	85 (^{m}9, ^{g}40)
C: Fe600 steel re-bars + Aluminum Foam (Type A) T: Fe330 hollow carbon steel tubes	90 (^{m}7, ^{g}35)
C: Fe600 steel re-bars + Aluminum Foam (Type B) T: Fe330 hollow carbon steel tubes	75 (^{m}5, ^{g}24)
C: Fe600 steel re-bars + Aluminum Foam (Type B2) T: Fe330 hollow carbon steel tubes	51 (^{m}12, ^{g}33)
C: Fe600 steel re-bars + Aluminum Foam (Type B3) T: Fe330 hollow carbon steel tubes	80 (^{m}5, ^{g}29)

$*^{m}$ Number of cracks developed $*^{g}$ Average depth of cracks (mm)

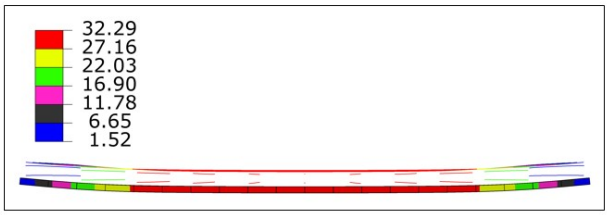

(a) C: Fe600 steel re-bars; T: Fe330 carbon steel tubes

(b) C: Fe330 carbon steel tubes; T: Fe600 steel re-bars

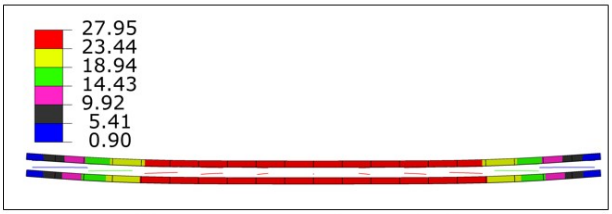

(c) C & T: Fe330 carbon steel tubes

Fig. 12. Distribution of deflection for the considered substitutions of the tubes under maximum blast pressure of 1.72 MPa

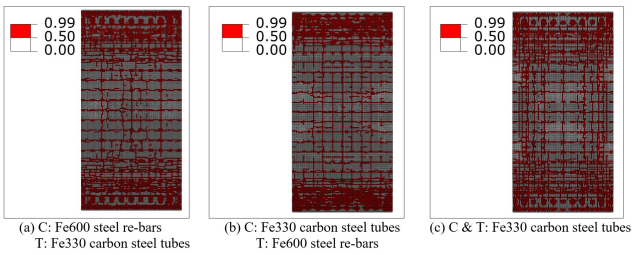

Fig. 13. Pattern of cracks on the bottom tension side of slab RC 4 for the considered substitutions of the steel tubes (red color: “damaged material”; white color: “undamaged material”)

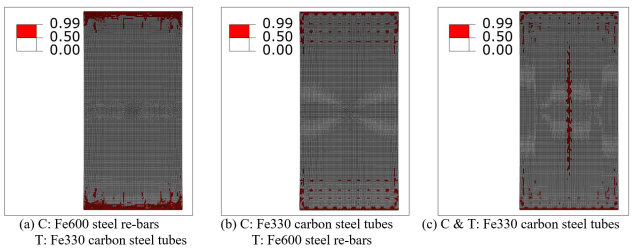

Fig. 14. Pattern of cracks on the impact side (top face) of slab RC 4 for the considered substitutions of the steel tubes (red color: “damaged material”; white color: “undamaged material”)

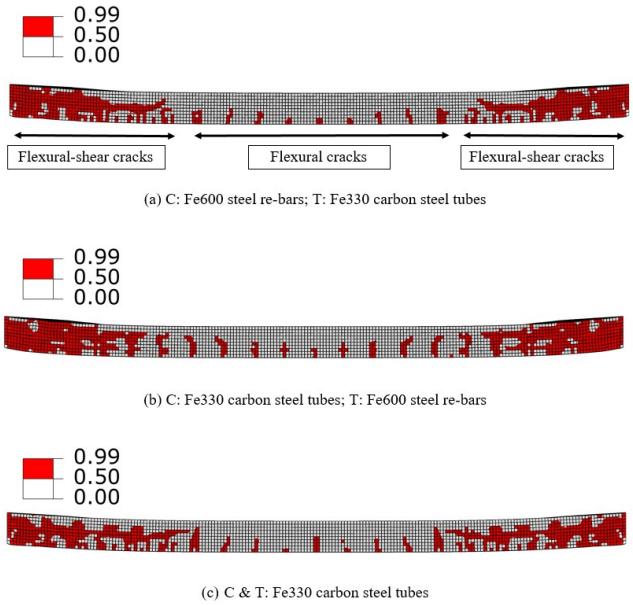

Fig. 15. Pattern of cracks along the span of slab RC 4 for the considered substitutions of the tubes

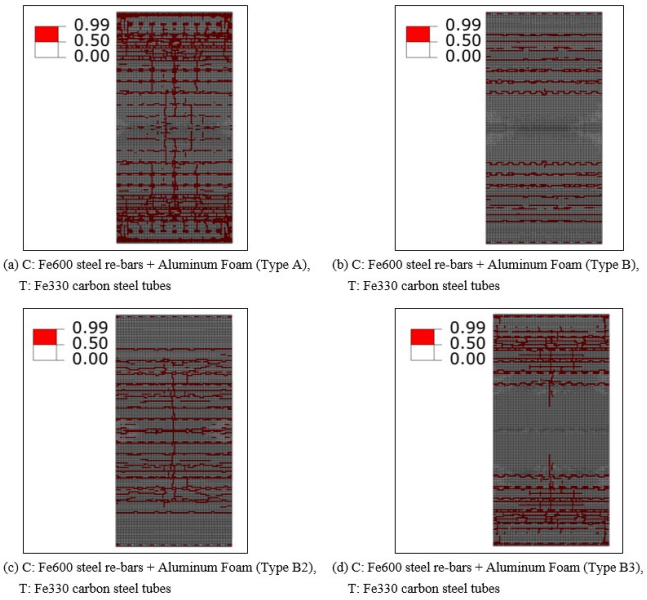

Fig. 16. Pattern of cracks on bottom tension side of slab RC 4 for the considered schemes of the aluminum foam

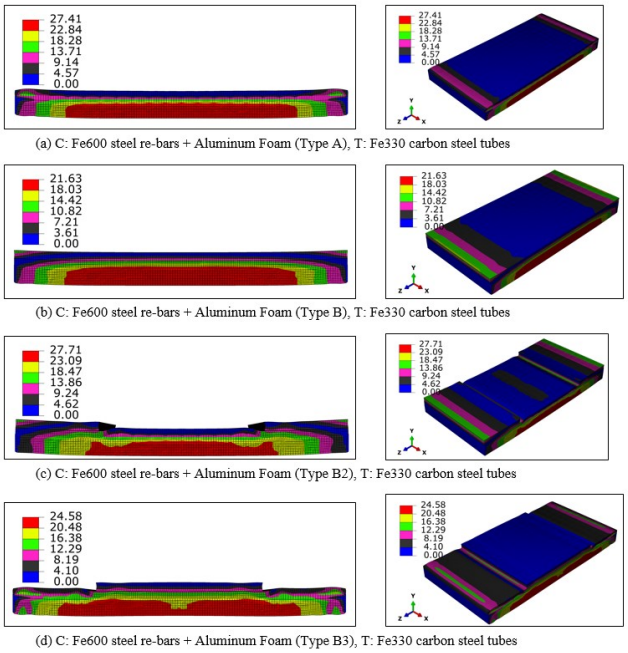

Fig. 17. Distribution of deflection (mm) in slab RC 4 for the considered schemes of the aluminum foam

4. Conclusions

Based on the analyses results, the following conclusions are obtained:

1. The concrete slab reinforced with the Fe600 steel re-bars on the compression side and the Fe330 carbon steel hollow tubes of equivalent strength on the tension side decreased the mid-span deflection by approximately 27%, damage dissipation energy by 42%, and depth of transverse flexural cracks by 42%, while the slab with the Fe330 carbon steel tubes on both sides reduced the mid-span deflection by 45%, damage dissipation energy by 48%, and depth of flexural cracks by 29% (approx..) in comparison to the slab with Fe600 steel re-bars on both sides. Although, reduction of deflection and damage dissipation energy is maximum for the complete replacement of the steel re-bars by the tubes on both the sides of the slab, yet full substitution by the tubes on the tension side only possess higher cracking resistance against the considered blast loading.
2. Minimum compression of a double layer of the aluminum foam with steel sheet on the compression face of the slab reinforced with the Fe600 steel re-bars and with the Fe330 carbon steel hollow tubes on the tension side has been obtained 3.61 mm (at mid-span) which is less than half of the minimum compression obtained with a single protected layer of the aluminum foam and sheet (9.24 mm). This shows that double aluminum foam layer not only improves the stiffness of the slab by controlling the deflection (21%) but also immensely enhance the damage dissipation energy (83%) of the slab as compared to the single aluminum foam layer.
3. The concrete slab reinforced with the conventional steel re-bars on the compression side fully covered with two protecting layers of the aluminum foam and steel sheet (Type B) and with the carbon steel hollow tubes of equivalent strength on the tension side gives the most superior performance out of the substitutions considered in this study against the considered blast loading.

Acknowledgement

The authors are grateful for helpful discussions with Professor T K Datta of the Department of Civil Engineering of Indian Institute of Technology Delhi (New Delhi, India-110 016).

Disclosures

Free Access to this article is sponsored by SARL ALPHA CRISTO INDUSTRIAL.

References

1. ABAQUS/CAE FEA program 2017. Concrete damaged plasticity model, explicit solver, three dimensional solid element library. ABAQUS DS-SIMULIA User Assistance Manual, 2017.
2. Brozda K, Selejdak J, and Kotes P. Analysis of properties of the FRP rebar to concrete structures. Applied Engineering Letters, 2017; 2(1): 6-10.
3. Bureau of Indian Standards. Criteria for blast resistant design of structures for explosions above ground. IS 4991(1968).
4. Castedo R, Segarra P, Alanon A, Lopez M L, Santos P A, Sanchidrian A J. Air blast resistance of full-scale slabs with different compositions: Numerical modeling and field validation. International Journal of Impact Engineering, 2015; 86: 145-156.
5. Chen C, Harte M A, and Fleck A N. The plastic collapse of sandwich beams with a metallic foam core. International Journal of Mechanical Sciences, 2001; 43: 1483-1506.
6. Feng J, Zhou Y, Wang P, Wang B, Zhou J, Chen H, Fan H, and Jin F. Experimental research on blast-resistance of one-way concrete slabs reinforced by BFRP bars under close-in explosion. Engineering Structures, 2017; 150: 550-561.
7. Gama A B, Bogetti A T, Fink K B, Yu J C, Claar D T, Eifert H H, Gillespie W J. Aluminum foam integral armor: a new dimension in armor design. Composite Structures, 2001; 52: 381-395.
8. Goel D M and Matsagar A V. Blast-resistant design of structures. Practice Periodical on Structural Design and Construction, 2014, ASCE, 19(2): 04014007-1-9.
9. Grassl P and Jirasek M. Damage-plastic model for concrete failure. International Journal of Solids and Structures, 2006; 43(22-23): 7166-7196.
10. Hanssen G A, Enstock L, and Langseth M. Close-range blast loading of aluminum foam panels. International Journal of Impact Engineering, 2002; 27: 593-618.
11. Hao H. Hao Y, Li J, and Chen W. Review of the current practices in blast-resistant analysis and design of concrete structures. Advances in Structural Engineering, 2016; 19(8): 1193-1223.

12. Hafezolghorani M, Hejazi F, Vaghei R, Jaafar B S M, and Karimzade K. Simplified damage plasticity model for concrete. Structural Engineering International, 2017; 27(1): 68-78.

13. Herwig A and Motavalli M. Axial behavior of square reinforced concrete columns strengthened with lightweight concrete elements and unbonded GFRP wrapping. Journal of Composites for Construction, 2012, ASCE, 16(6): 747-752.

14. Jason L, Huerta A, Cabot P G, Ghavamian S. An elastic plastic damage formulation for concrete: Application to elementary tests and comparison with an isotropic damage model. Computer Methods in Applied Mechanics and Engineering, 2006; 195(52): 7077-7092.

15. Joint Department of the Army, the Navy, and the Air Force. Structures to resist the effects of accidental explosions. Technical Manual, TM 5-1300(1990).

16. Ju W J. On energy-based coupled elastoplastic damage theories: Constitutive modeling and computational aspects. International Journal of Solids and Structures, 1989; 25(7): 803-833.

17. Kamde K D and Pillai G R. Effect of surface preparation on corrosion of steel rebars coated with cement-polymer-composites (CPC) and embedded in concrete. Construction and Building Materials, 2020; 237: 1-12.

18. Kumar V, Kartik V K, and Iqbal A M. Experimental and numerical investigation of reinforced concrete slabs under blast loading. Engineering Structures, 2020; 206: 110-125.

19. Lee J and Fenves L G. Plastic-damage model for cyclic loading of concrete structures. Journal of Engineering Mechanics, 1998, ASCE; 124(8).

20. Lin X, Zhang X Y, and Hazell J P. Modelling the response of reinforced concrete panels under blast loading. Materials & Design (1980-2015), 2014; 56: 620-628.

21. Low Y H and Hao H. Reliability analysis of direct shear and flexural failure modes of RC slabs under explosive loading. Engineering Structures, 2002; 24: 189-198.

22. Lubliner J, Oliver J, Oller S, and Onate E. A plastic-damage model for concrete. International Journal of Solids and Structures, 1989; 25(3): 299-326.

23. McCormack M T, Miller R, Kesler O, and Gibson J L. Failure of sandwich beams with metallic foam cores. International Journal of Solids and Structures, 2001; 38: 4901-4920.

24. Ohkubo K, Beppu M, Ohno T, and Satoh K. Experimental study on the effectiveness of fiber sheet reinforcement on the explosive-resistant performance of concrete plates. International Journal of Impact Engineering, 2008; 35: 1702-1708.

25. Schenker A, Anteby I, Gal E, Kivity Y, Nizri E, Sadot O, Michaelis R, Levintant O, Ben-Dor G. Full-scale field tests of concrete slabs subjected to blast loads. International Journal of Impact Engineering, Elsevier, 2008; 35: 184-198.

26. Seitzberger M, Rammerstorfer G F, Gradinger R, Degischer P H, Blaimschein M, and Walch C. Experimental studies on the quasi-static axial crushing of steel columns filled with aluminum foam. International Journal of Solids and Structures, 2000; 37: 4125-4147.

27. Silva F P and Lu B. Blast resistance capacity of reinforced concrete slabs. Journal of Structural Engineering, 2009, ASCE, 135(6).

28. Sim J, Park C, and Moon Y D. Characteristics of basalt fiber as a strengthening material for concrete structures. Composites: Part B, 2005; 36: 504-512.

29. Singh N D D and Ghosh R. Corrosion resistance performance of fusion bonded epoxy coated rebars. NSCP Conference, 2001; 113-121.

30. Soltani H, Khaloo A, and Sadraie H. Dynamic performance enhancement of RC slabs by steel fibers vs. externally bonded GFRP sheets under impact loading. Engineering Structures, 2020; 213: 1-21.

31. Tai S Y, Chu L T, Hu T H, Wu Y J. Dynamic response of a reinforced concrete slab subjected to air blast load. Theoretical and Applied Fracture Mechanics, 2011; 56(3): 140-147.

32. Tang F, Chen G, Brow K R, Volz S J, Koenigstein L M. Corrosion resistance and mechanism of steel rebar coated with three types of enamel. Corrosion Science, 2012; 59: 157-168.

33. Thiagarajan G, Kadambi V A, Robert S, and Johnson F C. Experimental and finite element analysis of doubly reinforced concrete slabs subjected to blast loads. International Journal of Impact Engineering, 2015; 75: 162-173.

34. Valentini B and Hofstetter G. Review and enhancement of 3D concrete models for large-scale numerical simulations of concrete structures. International Journal for Numerical and Analytical Methods in Geomechanics, 2011, Wiley; 37(3): 221-246.

35. Wang W, Zhang D, Lu F, Wang C S, and Tang F. Experimental study on scaling the explosion resistance of a one-way square reinforced concrete slab under a close-in blast loading. International Journal of Impact Engineering, 2012; 49: 158-164.

36. Wang W, Zhang D, Lu F, Wang C S, and Tang F. Experimental study and numerical simulation of the damage mode of a square reinforced concrete slab under close-in explosion. Engineering Failure Analysis, 2013; 27: 41-51.

37. Wu C and Hao H. Modeling of simultaneous ground shock and airblast pressure on nearby structures from surface explosions. International Journal of Impact Engineering, 2005; 31(6): 699-717.

38. Wu C, Oehlers J D, Rebentrost M, Leach J, and Whittaker S A. Blast testing of ultra-high performance fibre and FRP-retrofitted concrete slabs. Engineering Structures, 2009; 31: 2060-2069.

39. Xu K and Lu Y. Numerical simulation study of spallation in reinforced concrete plates subjected to blast loading. Computers & Structures, 2006; 84(5-6): 431-438.

40. Yao S, Zhang D, Chen X, Lu F, and Wang W. Experimental and numerical study on the dynamic response of RC slabs under blast loading. Engineering Failure Analysis, 2016; 66: 120-129.

41. Zhao F C and Chen Y J. Damage mechanism and mode of square reinforced concrete slab subjected to blast loading. Theoretical and Applied Fracture Mechanics, 2013; 63-64: 54-62.

42. Zhou Q X, Kuznetsov A V, Hao H, and Waschl J. Numerical prediction of concrete slab response to blast loading. International Journal of Impact Engineering, 2008; 35(10): 1186-1200.